

Electromagnetic Property Sensing Based on Diffusion Model in ISAC System

Yuhua Jiang, Feifei Gao, Shi Jin, and Tie Jun Cui

Abstract—Integrated sensing and communications (ISAC) has opened up numerous game-changing opportunities for future wireless systems. In this paper, we develop a novel ISAC scheme that utilizes the diffusion model to sense the electromagnetic (EM) property of the target in a predetermined sensing area. Specifically, we first estimate the sensing channel by using both the communications and the sensing signals echoed back from the target. Then we employ the diffusion model to generate the point cloud that represents the target and thus enables 3D visualization of the target’s EM property distribution. In order to minimize the mean Chamfer distance (MCD) between the ground truth and the estimated point clouds, we further design the communications and sensing beamforming matrices under the constraint of a maximum transmit power and a minimum communications achievable rate for each user equipment (UE). Simulation results demonstrate the efficacy of the proposed method in achieving high-quality reconstruction of the target’s shape, relative permittivity, and conductivity. Besides, the proposed method can sense the EM property of the target effectively in any position of the sensing area.

Index Terms—Electromagnetic (EM) property sensing, integrated sensing and communications (ISAC), diffusion model, generative artificial intelligence (GAI)

I. INTRODUCTION

Recently, the concept of integrated sensing and communications (ISAC) has attracted significant interest from academy and industry professionals, particularly for its potential in the sixth-generation (6G) wireless networks [1], [2]. Compared with the traditional frequency-division sensing and communications (FDSAC) approach that requires separate frequency bands and infrastructure for each function, ISAC could concurrently share time, frequency, power, and hardware resources for both communications and sensing functions, and is anticipated to outperform FDSAC in terms of spectrum utilization, energy efficiency, and hardware requirements [3]–[5]. Additionally, ISAC can be integrated with other emerging technologies, such as reconfigurable intelligent surfaces (RIS), to enhance the performance of sensing and communications systems [6].

With its numerous advantages, ISAC is expected to be crucial in a variety of emerging applications such as vehicle

to everything (V2X) [7], extended reality (XR) [8], smart homes [9], and digital twins that seamlessly connects the tangible world with its virtual counterpart in the realm of communications [10]. In contrast to the image-based digital twins that focus on shape and spatial positioning, the digital twins for communications systems are tasked with the intricate reconstruction of communications pathways and the management of channel-specific challenges. In addition to the location, velocity, and shape, the precise values of the electromagnetic (EM) property of real-world entities are also significant. These attributes are pivotal as they dictate the physical phenomena such as diffraction, reflection, and scattering of EM waves. Moreover, sensing the EM property is essential in human body examination, which meets the escalating needs in societal security and the medical field.

Although ISAC has demonstrated important achievements in localization [11], tracking [12], imaging [13], and various other applications [3]–[6], EM property sensing within ISAC framework has been barely studied. To the best of the authors’ knowledge, only two works [14], [15] implement EM property sensing through mesh-based methods. However, the methods in [14] and [15] only address 2D scenarios and are not suitable for 3D scenarios, because the computational cost and memory requirements in 3D scenarios escalate significantly. Additionally, the complexity of mesh generation and the need for more sophisticated meshing algorithms further complicate the extension of [14] and [15] to 3D scenarios.

Hence, reducing the complexity of ISAC algorithms in 3D scenarios is crucial to accurately reflecting the propagation of EM waves in the real world. Recent studies have applied the artificial intelligence (AI) algorithms in ISAC systems to address the high-computational-complexity problem. For instance, the work by Zhu et al. [16] proposed an AI-enabled STAR-RIS aided ISAC system for secure communications. Additionally, Zhu et al. [17] provided an overview of how AI can be pushed to the wireless network edge, highlighting the opportunities for integrated sensing, communications, and computation towards 6G. Moreover, Wen et al. [18] investigated task-oriented sensing, computation, and communications integration for multi-device edge AI. Wang et al. [19] explored the generative AI (GAI) in ISAC systems from the physical layer perspective.

However, transferring conventional AI methods to 3D EM property sensing presents specific challenges due to the ill-posed nature of the inverse problems involved in EM property sensing. Traditional AI methods may face significant hurdles when tasked with these complex inverse problems [20]. One of the primary difficulties is the high degree of

Y. Jiang and F. Gao are with Institute for Artificial Intelligence, Tsinghua University (THUAI), State Key Lab of Intelligent Technologies and Systems, Tsinghua University, Beijing National Research Center for Information Science and Technology (BNRist), Beijing, P.R. China (email: jiangyh20@mails.tsinghua.edu.cn, feifeigao@ieee.org).

S. Jin is with the National Mobile Communications Research Laboratory, Southeast University, Nanjing 210096, China (e-mail: jinshi@seu.edu.cn).

T. J. Cui is with the State Key Laboratory of Millimeter Waves, Southeast University, Nanjing 210096, China (e-mail: tjcui@seu.edu.cn).

non-linearity and the presence of multiple scattering effects in EM wave propagation. These factors contribute to the ill-posedness of the problem, making it difficult to accurately infer the underlying EM property from the observed data. Traditional AI models exhibit high computational complexity, poor solution effectiveness, and significant sensitivity to noise when addressing complex EM inverse scattering problems [21]. Moreover, small errors in the input data can lead to large deviations in the estimated EM property, which is particularly problematic for traditional AI methods. This sensitivity to noise and measurement errors can yield unreliable or inconsistent results, undermining the effectiveness of EM property sensing in practical applications.

One promising AI approach to overcome these challenges is the diffusion model. Recently, GAI has become increasingly popular due to its versatility and capability to perform a wide range of tasks. Among the GAI models, the diffusion model stands out as a particularly effective approach. Unlike other GAI methods, the diffusion model offers enhanced flexibility and efficiency, making it well-suited for EM property sensing [22], [23]. The diffusion model's robustness to noise ensures accurate data collection, while its adaptability allows the model to be fine-tuned for various applications. The diffusion model's efficiency is crucial for real-time processing, and its scalability handles large datasets effectively. Moreover, diffusion models can integrate prior knowledge and capture complex relationships, which provides a comprehensive understanding of EM property. Their continuous learning capability and compatibility with other technologies make them versatile tools in the field of EM property sensing.

In this paper, we develop a novel ISAC scheme that leverages the diffusion model to accurately sense the EM property of a target within a predetermined sensing area. We first utilize both communications and sensing signals that are reflected back from the target to estimate the sensing channel. Once the sensing channel is estimated, we employ the diffusion model to generate a detailed point cloud representation of the target. This point cloud provides a clear 3D visualization of the EM property distribution, including critical parameters such as shape, relative permittivity, and conductivity. To ensure high fidelity in these visualizations, we design the communications and sensing beamforming matrices to minimize the mean Chamfer distance between the ground truth and the estimated point clouds. This optimization is performed under the constraints of a maximum transmit power and a minimum achievable communications rate for each user equipment (UE). Simulation results validate the efficacy of the proposed method and demonstrate its capability to achieve high-quality reconstruction of the target's EM property. Additionally, the proposed method proves to be effective in sensing the EM property of the target regardless of its position within the sensing area. This robustness highlights the potential of the proposed ISAC scheme to be applied in various practical scenarios where precise EM property sensing is required.

The rest of this paper is organized as follows. Section II presents the ISAC system model. Section III elaborates the formulation of EM scattering. Section IV describes the diffusion probabilistic model for EM property sensing. Sec-

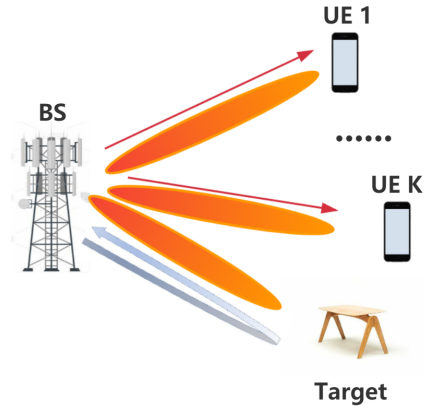


Fig. 1. The system model for simultaneous communications information transmission and EM property sensing.

tion V proposes the approach to designing the beamforming matrices with tradeoff between sensing and communications. Section VI provides the numerical simulation results, and Section VII draws the conclusion.

Notations: Boldface denotes a vector or a matrix; j corresponds to the imaginary unit; $(\cdot)^H$, $(\cdot)^\top$, and $(\cdot)^*$ represent Hermitian, transpose, and conjugate, respectively; \odot denotes the Hadamard product; \otimes denotes the Kronecker product; $\text{vec}(\cdot)$ and $\text{unvec}(\cdot)$ denote the vectorization and unvectorization operation; ∇ denotes the nabla operator; $\text{diag}(\mathbf{a})$ denotes the diagonal matrix whose diagonal elements are the elements of \mathbf{a} ; \mathbf{I} denote the identity matrix with compatible dimensions; $\|\mathbf{a}\|_2$ denotes ℓ_2 -norm of the vector \mathbf{a} ; $\|\mathbf{A}\|_F$ denotes Frobenius-norm of the matrix \mathbf{A} ; $\text{tr}(\mathbf{A})$ denotes the trace of the matrix \mathbf{A} ; $|\cdot|$ denotes the element-wise absolute value of complex vectors or matrices; $\mathbf{A} \succeq \mathbf{0}$ indicates that the matrix \mathbf{A} is positive semi-definite; the distribution of a real-valued Gaussian random vector with mean $\boldsymbol{\mu}$ and covariance matrix \mathbf{A} is denoted as $\mathcal{N}(\boldsymbol{\mu}, \mathbf{A})$; the distribution of a circularly symmetric complex Gaussian (CSCG) random vector with mean $\boldsymbol{\mu}$ and covariance matrix \mathbf{A} is denoted as $\mathcal{CN}(\boldsymbol{\mu}, \mathbf{A})$.

II. SYSTEM MODEL

As illustrated in Fig. 1, consider a multi-antenna ISAC system for simultaneous information transmission and the target's EM property sensing. The system includes a base station (BS) equipped with N_t transmitting antennas and N_r receiving antennas, K UEs each equipped with a single antenna, as well as a target to be sensed. The BS transmits communications signals to the K UEs simultaneously and utilizes the received echo signals to sense the EM property of the target. The scenario is also known as the mono-static ISAC system.

The BS adopts fully digital precoding structure where the number of RF chains N_{RF} is equal to the number of antennas N_t . The frequency of the signals is denoted by f , and the length of the transmitted symbols is denoted by L . We assume a quasi-static environment where the communications and sensing channels remain unchanged throughout the ISAC period.

Suppose the l -th transmit signal at the BS is expressed as

$$\begin{aligned} \mathbf{x}(l) &= \mathbf{W}_s \mathbf{s}(l) + \mathbf{W}_c \mathbf{c}(l) \\ &= [\mathbf{W}_s, \mathbf{W}_c] [\mathbf{s}(l)^\top, \mathbf{c}(l)^\top]^\top = \mathbf{W} \hat{\mathbf{x}}(l), \end{aligned} \quad (1)$$

where $\mathbf{s}(l) \in \mathbb{C}^{N_t \times 1}$ denotes the dedicated sensing signal and $\mathbf{c}(l) \in \mathbb{C}^{K \times 1}$ denotes the transmission symbols intended to K UEs. Moreover, $\mathbf{W}_s = [\mathbf{w}_{s,1}, \mathbf{w}_{s,2}, \dots, \mathbf{w}_{s,N_t}] \in \mathbb{C}^{N_r \times N_t}$ and $\mathbf{W}_c = [\mathbf{w}_{c,1}, \mathbf{w}_{c,2}, \dots, \mathbf{w}_{c,K}] \in \mathbb{C}^{N_r \times K}$ represent the digital beamforming matrices for sensing and communications, respectively. Besides, $\mathbf{W} = [\mathbf{W}_s, \mathbf{W}_c]$ denotes the equivalent transmit beamforming matrix. We assume that the sensing signal is generated pseudo-randomly, which satisfies $\mathbb{E}[\mathbf{s}(l)] = \mathbf{0}$ and $\mathbb{E}[\mathbf{s}(l)\mathbf{s}^H(l)] = \mathbf{I}_{N_t}$. We also assume that the transmitted communications symbol $\mathbf{c}(l)$ satisfies $\mathbf{c}(l) \sim \mathcal{CN}(\mathbf{0}, \mathbf{I}_K)$, while the sensing and communications signals are mutually uncorrelated. Thus, the transmit signal covariance matrix is given by

$$\mathbf{S}_x = \mathbb{E}[\mathbf{x}(l)\mathbf{x}^H(l)] = \mathbf{W}\mathbf{W}^H = \mathbf{R}_s + \sum_{k=1}^K \mathbf{R}_k, \quad (2)$$

where the Gram matrix for the dedicated sensing is defined as $\mathbf{R}_s \triangleq \mathbf{W}_s \mathbf{W}_s^H$, and the rank-one Gram matrix for the k -th UE's communications is defined as $\mathbf{R}_k \triangleq \mathbf{w}_{c,k} \mathbf{w}_{c,k}^H$.

Assume that the BS operates under a maximum transmit power P , i.e., $\text{tr}(\mathbf{S}_x) \leq P$. Let $\mathbf{X} = [\mathbf{x}(1), \dots, \mathbf{x}(L)]$ denote the transmitted signal over L symbols. By assuming that L is sufficiently large, the sample covariance matrix of \mathbf{X} can be approximated as the statistical covariance matrix \mathbf{S}_x , i.e., $\frac{1}{L} \mathbf{X}\mathbf{X}^H \approx \mathbf{S}_x$.

A. Communications Model

Assume each UE is equipped with a single antenna. Let $\mathbf{h}_k \in \mathbb{C}^{N_r \times 1}$ denote the channel vector from the BS to the k -th UE. The received signal at the k -th UE without sensing interference cancellation is given by

$$y_k(l) = \mathbf{h}_k^H \mathbf{x}(l) + z_k(l), \quad l = 1, \dots, L, \quad (3)$$

where $z_k(l) \sim \mathcal{CN}(0, \sigma_k^2)$ denotes the noise at the k -th UE. Based on the received signal in (3), the received signal-to-interference-plus-noise ratio (SINR) at the k -th UE is

$$\gamma_k = \frac{\mathbf{h}_k^H \mathbf{R}_k \mathbf{h}_k}{\sigma_k^2 + \mathbf{h}_k^H (\mathbf{R}_s + \sum_{k' \neq k} \mathbf{R}_{k'}) \mathbf{h}_k}. \quad (4)$$

Substituting (2) into (4), the achievable rate of the communications channel for the k -th UE with multi-UE and sensing interference is given by

$$R_k = \log_2 \left(1 + \frac{\mathbf{h}_k^H \mathbf{R}_k \mathbf{h}_k}{\sigma_k^2 + \mathbf{h}_k^H (\mathbf{S}_x - \mathbf{R}_k) \mathbf{h}_k} \right). \quad (5)$$

B. Sensing Model

Assume the BS adopts its N_r receiving antennas to obtain the echo signals and then estimates the EM property of the target. In this case, the received target echo signals at the BS is expressed as

$$\mathbf{Y} = \mathbf{H}_s \mathbf{X} + \mathbf{Z}, \quad (6)$$

where $\mathbf{Y} = [\mathbf{y}(1), \dots, \mathbf{y}(L)]$, $\mathbf{Z} = [\mathbf{z}(1), \dots, \mathbf{z}(L)]$ denotes the noise at the BS receiver with $\mathbf{z}(l) \sim \mathcal{CN}(\mathbf{0}, \sigma_s^2 \mathbf{I}_{N_r})$, and \mathbf{H}_s denotes the sensing channel matrix. Let us vectorize (6) as

$$\tilde{\mathbf{y}} = (\mathbf{X}^\top \otimes \mathbf{I}_{N_r}) \tilde{\mathbf{h}}_s + \tilde{\mathbf{z}}, \quad (7)$$

where $\tilde{\mathbf{y}} = \text{vec}(\mathbf{Y}) \in \mathbb{C}^{N_r L \times 1}$, $\tilde{\mathbf{h}}_s = \text{vec}(\mathbf{H}_s) \in \mathbb{C}^{N_r N_t \times 1}$, and $\tilde{\mathbf{z}} = \text{vec}(\mathbf{Z}) \in \mathbb{C}^{N_r L \times 1}$. It follows from (7) that $\tilde{\mathbf{y}} \sim \mathcal{CN}((\mathbf{X}^\top \otimes \mathbf{I}_{N_r}) \tilde{\mathbf{h}}_s, \sigma_s^2 \mathbf{I}_{LN_r})$.

In order to extract the EM property of the target, the BS first needs to estimate $N_r N_t$ complex parameters in $\tilde{\mathbf{h}}_s$ or \mathbf{H}_s . It has been proven in [24] that the Cramér-Rao bound (CRB) matrix of $\tilde{\mathbf{h}}_s$ is

$$\begin{aligned} \text{CRB} &= [(\mathbf{X}^\top \otimes \mathbf{I}_{N_r})^H (\sigma_s^2 \mathbf{I}_{LN_r})^{-1} (\mathbf{X}^\top \otimes \mathbf{I}_{N_r})]^{-1} \\ &= \sigma_s^2 (\mathbf{X}^* \mathbf{X}^\top \otimes \mathbf{I}_{N_r})^{-1} \stackrel{(a)}{=} \frac{\sigma_s^2}{L} (\mathbf{S}_x^\top \otimes \mathbf{I}_{N_r})^{-1}, \end{aligned} \quad (8)$$

where $\stackrel{(a)}{=}$ comes from the approximation $\frac{1}{L} \mathbf{X}\mathbf{X}^H \approx \mathbf{S}_x$. We then adopt the trace of CRB as the scalar criterion to estimate $\tilde{\mathbf{h}}_s$, i.e.,

$$\text{tr}(\text{CRB}) = \frac{N_r \sigma_s^2}{L} \text{tr}(\mathbf{S}_x^{-1}). \quad (9)$$

The least square (LS) method is applied as

$$\hat{\tilde{\mathbf{h}}}_s = (\mathbf{X}^* \mathbf{X}^\top \otimes \mathbf{I}_{N_r})^{-1} (\mathbf{X}^\top \otimes \mathbf{I}_{N_r})^H \tilde{\mathbf{y}}, \quad (10)$$

and there is $\hat{\tilde{\mathbf{h}}}_s \sim \mathcal{CN}(\tilde{\mathbf{h}}_s, \sigma_s^2 (\mathbf{X}^* \mathbf{X}^\top \otimes \mathbf{I}_{N_r})^{-1})$. Consequently, $\hat{\mathbf{H}}_s = \text{unvec}(\hat{\tilde{\mathbf{h}}}_s)$ is the minimum variance unbiased estimated sensing channel that can achieve the CRB in (8).

III. EM SCATTERING FORMULATION

Assume the EM property of the target is isotropic. Sensing the EM property involves reconstructing the contrast function $\chi(\mathbf{r})$ defined as the difference in complex relative permittivity between the target and the background medium (the air here). Given that the relative permittivity and conductivity of air are approximately equal to 1 and 0 Siemens/meter (S/m), we can formulate the contrast function [25], [26] as

$$\chi(\mathbf{r}) = \epsilon_r(\mathbf{r}) - \frac{j\sigma(\mathbf{r})}{\epsilon_0 \omega} - 1, \quad (11)$$

where $\epsilon_r(\mathbf{r})$ denotes the real relative permittivity at point \mathbf{r} , $\sigma(\mathbf{r})$ denotes the conductivity at point \mathbf{r} , $\omega = 2\pi f$ denotes the angular frequency of the EM waves, and ϵ_0 is the vacuum permittivity. We then aim to reconstruct the distributions of both $\epsilon_r(\mathbf{r})$ and $\sigma(\mathbf{r})$.

Assume the electric fields have an $e^{-j\omega t}$ time dependence throughout the paper. Let $\lambda = c/f$ denote the wavelength and $k_b = 2\pi/\lambda$ denote the wave number in the background medium. Let $\mathbf{E}^t(\mathbf{r}) \in \mathbb{C}^{3 \times 1}$ and $\mathbf{E}^i(\mathbf{r}) \in \mathbb{C}^{3 \times 1}$ denote the total electric field and the incident electric field in x , y , and z axis, respectively. When the target is illuminated by an incident field $\mathbf{E}^i(\mathbf{r})$, $\mathbf{E}^t(\mathbf{r})$ and $\mathbf{E}^r(\mathbf{r})$ will satisfy the homogeneous and inhomogeneous vectorial wave equations, respectively [27]:

$$\nabla \times \nabla \times \mathbf{E}^i(\mathbf{r}) - k_b^2 \mathbf{E}^i(\mathbf{r}) = \mathbf{0}, \quad (12)$$

$$\nabla \times \nabla \times \mathbf{E}^t(\mathbf{r}) - k_b^2 \mathbf{E}^t(\mathbf{r}) = k_b^2 \chi(\mathbf{r}) \mathbf{E}^i(\mathbf{r}). \quad (13)$$

Suppose the target is located within the region D . In order to solve (12) and (13), the total electric field within D can be formulated by the 3D Lippmann-Schwinger equation as [27]–[29]

$$\mathbf{E}^t(\mathbf{r}) = \mathbf{E}^i(\mathbf{r}) + k_b^2 \iiint_D \overline{\overline{\mathbf{G}}}(\mathbf{r}, \mathbf{r}') \chi(\mathbf{r}') \mathbf{E}^t(\mathbf{r}') d\mathbf{r}', \quad (14)$$

where $\overline{\overline{\mathbf{G}}}(\mathbf{r}, \mathbf{r}') \in \mathbb{C}^{3 \times 3}$ is the dyadic electric field Green's function that satisfies

$$\nabla \times \nabla \times \overline{\overline{\mathbf{G}}}(\mathbf{r}, \mathbf{r}') - k_b^2 \overline{\overline{\mathbf{G}}}(\mathbf{r}, \mathbf{r}') = \mathbf{I}_3 \delta(\mathbf{r} - \mathbf{r}'). \quad (15)$$

Meanwhile, $\overline{\overline{\mathbf{G}}}(\mathbf{r}, \mathbf{r}')$ can be formulated as [30]

$$\begin{aligned} \overline{\overline{\mathbf{G}}}(\mathbf{r}, \mathbf{r}') &= \left(\mathbf{I}_3 + \frac{\nabla \nabla}{k_b^2} \right) g(\mathbf{r}, \mathbf{r}') \\ &= \left[\left(\frac{3}{k_b^2 R'^2} - \frac{3j}{k_b R'} - 1 \right) \hat{\mathbf{r}} \hat{\mathbf{r}}^\top - \left(\frac{1}{k_b^2 R'^2} - \frac{j}{k_b R'} - 1 \right) \mathbf{I}_3 \right] g(\mathbf{r}, \mathbf{r}'). \end{aligned} \quad (16)$$

In (16), R' is the distance defined as $R' \triangleq \|\mathbf{r} - \mathbf{r}'\|_2$, $\hat{\mathbf{r}} \in \mathbb{R}^{3 \times 1}$ is defined as the unit vector from \mathbf{r}' to \mathbf{r} , and $g(\mathbf{r}, \mathbf{r}')$ is the scalar Green's function defined as $g(\mathbf{r}, \mathbf{r}') \triangleq \frac{\exp(jk_b R')}{4\pi R'}$ [30].

The echo electric field at the BS's receiver scattered back from the target can then be formulated as [28], [29]

$$\mathbf{E}^s(\mathbf{r}_n) = k_b^2 \iiint_D \overline{\overline{\mathbf{G}}}(\mathbf{r}_n, \mathbf{r}') \chi(\mathbf{r}') \mathbf{E}^t(\mathbf{r}') d\mathbf{r}', \quad (17)$$

where \mathbf{r}_n denotes the position of the n -th receiving antenna. Suppose the receiver can only measure the scalar electric field component in the direction represented by the unit vector $\hat{\mathbf{p}} \in \mathbb{R}^{3 \times 1}$. The received echo signals can be formulated as

$$\mathbf{y} = G_r [\mathbf{E}^s(\mathbf{r}_1), \dots, \mathbf{E}^s(\mathbf{r}_{N_r})]^\top \hat{\mathbf{p}} + \mathbf{z}, \quad (18)$$

where G_r is the receiving antenna gain. According to (14), (17), and (18), the EM property of the target is implicitly encoded in the received echo signals that are transmitted through the sensing channel. Thus, we can leverage the estimated sensing channel matrix as the prior information to reconstruct the EM property of the target.

IV. DIFFUSION PROBABILISTIC MODEL FOR EM PROPERTY SENSING

From the 3D formulation of EM scattering (14)–(18), we can sense the EM property of the target using inversion techniques [20], [21], [31]. When employing the traditional mesh-based inversion techniques, the spatial arrangement of voxels is typically predetermined, which requires a comprehensive analysis of the entire domain of interest (DoI) to ascertain the EM property of the target. The mesh-based approach, while thorough, incurs a significant computational cost due to the over-resolution of the background medium, which is not the focus of our interest. Moreover, the results yielded by the 3D mesh-based inversion methods are not inherently conducive to direct visualization. On the other hand, the use of the point cloud methodology offers a more efficient and straightforward alternative to sense the EM property. Point clouds inherently allow for the separation of the background medium from the target, which thus obviates the need to analyze the known

background medium and substantially cuts down the computational overhead. Moreover, the representation of data through the point cloud enables a clear and immediate visualization of the 3D target, which facilitates a more intuitive interpretation of the inversion results.

Define the i -th normalized non-dimensional 5D point $\mathbf{x}_i^{(0)} \in \mathbb{R}^{5 \times 1}$ that comprises both the 3D location information and the 2D EM property as

$$\mathbf{x}_i^{(0)} = \left[\frac{x_i - x_c}{x_d}, \frac{y_i - y_c}{y_d}, \frac{z_i - z_c}{z_d}, \frac{\epsilon_i}{\epsilon_0}, \frac{\sigma_i}{\epsilon_0 \omega} \right]^\top, \quad (19)$$

where $x_i, y_i,$ and z_i denote the coordinates of the i -th point in each dimension; $x_c, y_c,$ and z_c denote the coordinates of the center of the target; $x_d, y_d,$ and z_d denote the characteristic length of each dimension that can be selected as the corresponding standard deviations without loss of generality.

Suppose the target can be represented by a 5D point cloud $\mathcal{X}^{(0)} = \{\mathbf{x}_i^{(0)}\}_{i=1}^N$, consisting of N non-dimensional points with the corresponding EM property in (19). The 5D point cloud behaves like a collection of particles within an evolving thermodynamic system over time. Each point $\mathbf{x}_i^{(0)}$ in the point cloud is treated as being independently sampled from the point distribution, which will be denoted as $q(\mathbf{x}_i^{(0)} | \hat{\mathbf{H}}_s)$. Here, $\hat{\mathbf{H}}_s$ is considered as the prior condition that determines the distribution of $\mathbf{x}_i^{(0)}$.

A. Forward Diffusion Process

In the forward diffusion process, the original point cloud distribution progressively transitions into a noise distribution. Let $\mathbf{x}_i^{(1:T)}$ denote the set of $\mathbf{x}_i^{(1)}, \dots, \mathbf{x}_i^{(T)}$ that are sequentially generated from $\mathbf{x}_i^{(0)}$ with the maximum time step T . The forward diffusion process can be deliberately modeled as a Markov chain, i.e.,

$$q(\mathbf{x}_i^{(1:T)} | \mathbf{x}_i^{(0)}) = \prod_{t=1}^T q(\mathbf{x}_i^{(t)} | \mathbf{x}_i^{(t-1)}), \quad (20)$$

where $q(\mathbf{x}_i^{(t)} | \mathbf{x}_i^{(t-1)})$ represents the probability transition function, which simulates the evolution of point distributions from one time step to the next by incorporating noise into the current distribution.

Since each point in the point cloud is independently sampled from $q(\mathbf{x}_i^{(0)} | \hat{\mathbf{H}}_s)$, the probability distribution of the overall point cloud is the product of the probability distribution of each point, i.e.,

$$q(\mathcal{X}^{(1:T)} | \mathcal{X}^{(0)}) = \prod_{i=1}^N q(\mathbf{x}_i^{(1:T)} | \mathbf{x}_i^{(0)}). \quad (21)$$

The point distribution at each time step is assumed to follow a Gaussian distribution. Consequently, the transition probability function, which describes the noise addition in each time step, can be expressed as

$$q(\mathbf{x}_i^{(t)} | \mathbf{x}_i^{(t-1)}) = \mathcal{N}(\mathbf{x}_i^{(t)} | \sqrt{1 - \beta_t} \mathbf{x}_i^{(t-1)}, \beta_t \mathbf{I}), \quad (22)$$

where β_1, \dots, β_T are linearly increasing hyperparameters that govern the diffusion intensity at each subsequent time step during the forward diffusion process.

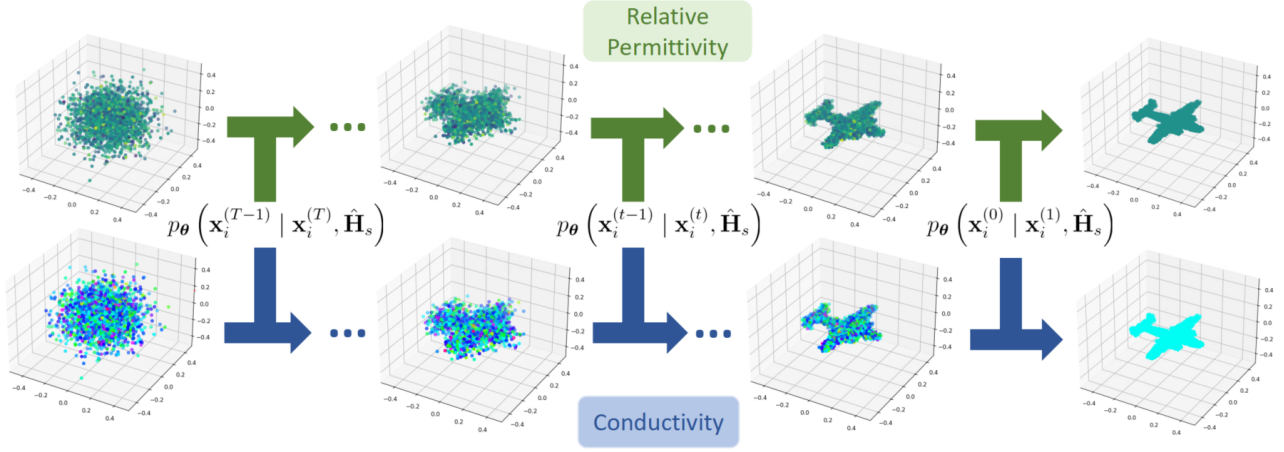


Fig. 2. The reverse diffusion process guided by the estimated sensing channel as the prior information. The shape, relative permittivity, and conductivity of the target are reconstructed simultaneously.

Referring to (22), once the diffusion process between adjacent time steps is complete, it is possible to trace the transformation of the target from the initial state to any subsequent time step. However, performing such iterative calculations for each time step during the training process is time-consuming and inefficient. By applying the Bayes' rule and using the renormalization technique, (22) can be transformed to directly facilitate the calculation of the state of the point cloud at an arbitrary time step as

$$q(\mathbf{x}_i^{(t)}) = \mathcal{N}\left(\sqrt{\bar{\alpha}_t}\mathbf{x}_i^{(0)}, (1 - \bar{\alpha}_t)\mathbf{I}\right), \quad (23)$$

where $\alpha_t \triangleq 1 - \beta_t$ and $\bar{\alpha}_t \triangleq \prod_{p=1}^t \alpha_p$. The equation (23) provides the relationship between the intermediate state at any time step t and the initial state, which significantly simplifies the calculation process.

B. Reverse Diffusion Process

In this subsection, we aim to reconstruct the 5D point cloud representation of the target and the EM property of each point from the estimated sensing channel through the reverse diffusion process, which is analogous to the Langevin dynamics sampling procedures [32]. In the reverse process, we can reformulate (23) as

$$\mathbf{x}_i^{(0)} = \frac{1}{\sqrt{\bar{\alpha}_t}} \left(\mathbf{x}_i^{(t)} - \sqrt{1 - \bar{\alpha}_t} \boldsymbol{\epsilon}_i^{(t)} \right), \quad \boldsymbol{\epsilon}_i^{(t)} \sim \mathcal{N}(\mathbf{0}, \mathbf{I}). \quad (24)$$

Thus, $\mathbf{x}_i^{(0)}$ can be estimated by denoising $\mathbf{x}_i^{(t)}$ through a sequential process.

Similar to the forward diffusion process (20), the reverse diffusion process can also be modeled as a Markov chain conditioned on the estimated sensing channel, i.e.,

$$p_{\theta}(\mathbf{x}_i^{(0:T)} | \hat{\mathbf{H}}_s) = p(\mathbf{x}_i^{(T)}) \prod_{t=1}^T p_{\theta}(\mathbf{x}_i^{(t-1)} | \mathbf{x}_i^{(t)}, \hat{\mathbf{H}}_s). \quad (25)$$

At the beginning of the reverse process, we start with N points sampled from a predetermined Gaussian distribution

$p(\mathbf{x}_i^{(T)})$ that approximates $q(\mathbf{x}_i^{(T)})$, which serves as the initial input. These initial points are subsequently processed through the reverse Markov chain to ultimately delineate the original 5D point cloud. Similar to (21), there is

$$p_{\theta}(\mathcal{X}^{(0:T)} | \hat{\mathbf{H}}_s) = \prod_{i=1}^N p_{\theta}(\mathbf{x}_i^{(0:T)} | \hat{\mathbf{H}}_s). \quad (26)$$

In contrast to the learning-free forward diffusion process, the reverse diffusion process is learning-dependent. The diffusion model progressively retrieves the 5D point cloud constituting the target by sequentially denoising the initial Gaussian noise state. The shape, relative permittivity, and conductivity of the target are reconstructed simultaneously by the estimated sensing channel information as shown in Fig. 2. Similarly to the forward diffusion process, the transition probability function in the reverse process can be articulated as

$$p_{\theta}(\mathbf{x}_i^{(t-1)} | \mathbf{x}_i^{(t)}, \hat{\mathbf{H}}_s) = \mathcal{N}\left(\mathbf{x}_i^{(t-1)} | \boldsymbol{\mu}_{\theta}(\mathbf{x}_i^{(t)}, t, \hat{\mathbf{H}}_s), \beta_t \mathbf{I}\right), \quad (27)$$

where $\boldsymbol{\mu}_{\theta}(\mathbf{x}_i^{(t)}, t, \hat{\mathbf{H}}_s)$ is the estimated mean implemented by a neural network parameterized by θ . The covariance matrix of the added noise at time step $t - 1$ is obtained based on the schedule in the forward diffusion process. The corresponding estimated sensing channel $\hat{\mathbf{H}}_s$, the point cloud representation of the target's EM property at time step t , and the current time step t serve as conditions that enable the neural network to ascertain the mean of distribution at time step $t - 1$. This, in turn, aids to determine the state of the point cloud at time step $t - 1$. By reversing the forward diffusion process, we establish the precise mathematical expression of $q(\mathbf{x}_i^{(t-1)} | \mathbf{x}_i^{(t)}, \mathbf{x}_i^{(0)})$ with the following closed-form Gaussian distribution

$$q(\mathbf{x}_i^{(t-1)} | \mathbf{x}_i^{(t)}, \mathbf{x}_i^{(0)}) = \mathcal{N}\left(\mathbf{x}_i^{(t-1)} | \boldsymbol{\mu}_t(\mathbf{x}_i^{(t)}, \mathbf{x}_i^{(0)}), \gamma_t \mathbf{I}\right), \quad (28)$$

Algorithm 1 5D Point Cloud Estimation

Input : Estimated sensing channel $\hat{\mathbf{H}}_s$ corresponding to $\hat{\mathcal{X}}^{(0)}$, $p_\theta(\cdot|\cdot, \cdot)$, and T

- 1: Sample $\mathcal{X}^{(T)} \sim \mathcal{N}(\mathbf{0}, \mathbf{I})$
- 2: **for** $t = T, \dots, 1$ **do**
- 3: Sample $\hat{\mathcal{X}}^{(t-1)} \sim p_\theta(\hat{\mathcal{X}}^{(t-1)}|\hat{\mathcal{X}}^{(t)}, \hat{\mathbf{H}}_s)$
- 4: **end for**
- 5: **return** $\hat{\mathcal{X}}^{(0)}$

where the mean and the covariance are calculated according to the Bayes' rule as [23]

$$\boldsymbol{\mu}_t(\mathbf{x}_i^{(t)}, \mathbf{x}_i^{(0)}) = \frac{\sqrt{\bar{\alpha}_t} \beta_t}{1 - \bar{\alpha}_t} \mathbf{x}_i^{(0)} + \frac{\sqrt{\bar{\alpha}_t} (1 - \bar{\alpha}_{t-1})}{1 - \bar{\alpha}_t} \mathbf{x}_i^{(t)}, \quad (29)$$

$$\gamma_t = \frac{1 - \bar{\alpha}_{t-1}}{1 - \bar{\alpha}_t} \beta_t. \quad (30)$$

Substituting (24) into (29), there is

$$\boldsymbol{\mu}_t(\mathbf{x}_i^{(t)}, \mathbf{x}_i^{(0)}) = \frac{1}{\sqrt{\bar{\alpha}_t}} \left(\mathbf{x}_i^{(t)} - \frac{\beta_t}{\sqrt{1 - \bar{\alpha}_t}} \boldsymbol{\epsilon}_i^{(t)} \right), \boldsymbol{\epsilon}_i^{(t)} \sim \mathcal{N}(\mathbf{0}, \mathbf{I}). \quad (31)$$

The procedure to estimate the 5D point cloud $\hat{\mathcal{X}}^{(0)}$ is summarized in Algorithm 1.

C. Variational Lower Bound Maximization

The training goal in the reverse diffusion process is to maximize the log-likelihood function expectation of the 5D point cloud with EM property, expressed as $\mathbb{E}_{q(\mathbf{x}_i^{(0)})} [\ln p_\theta(\mathbf{x}_i^{(0)} | \hat{\mathbf{H}}_s)]$. However, direct optimization of the log-likelihood function expectation is impractical. Instead, we can maximize the variational lower bound (VLB)¹ of $\mathbb{E}_{q(\mathbf{x}_i^{(0)})} [\ln p_\theta(\mathbf{x}_i^{(0)} | \hat{\mathbf{H}}_s)]$, derived as

$$\begin{aligned} & \mathbb{E}_{q(\mathbf{x}_i^{(0)})} \ln p_\theta(\mathbf{x}_i^{(0)} | \hat{\mathbf{H}}_s) \\ &= \mathbb{E}_{q(\mathbf{x}_i^{(0)})} \ln \left[\mathbb{E}_{q(\mathbf{x}_i^{(1:T)} | \mathbf{x}_i^{(0)})} \frac{p_\theta(\mathbf{x}_i^{(0)} | \hat{\mathbf{H}}_s)}{q(\mathbf{x}_i^{(1:T)} | \mathbf{x}_i^{(0)})} \right] \\ &\stackrel{(a)}{\geq} \mathbb{E}_{q(\mathbf{x}_i^{(0)})} \mathbb{E}_{q(\mathbf{x}_i^{(1:T)} | \mathbf{x}_i^{(0)})} \ln \left[\frac{p_\theta(\mathbf{x}_i^{(0)} | \hat{\mathbf{H}}_s)}{q(\mathbf{x}_i^{(1:T)} | \mathbf{x}_i^{(0)})} \right] \\ &= \mathbb{E}_{q(\mathbf{x}_i^{(0:T)})} \ln \left[\frac{p_\theta(\mathbf{x}_i^{(0:T)} | \hat{\mathbf{H}}_s)}{q(\mathbf{x}_i^{(1:T)} | \mathbf{x}_i^{(0)})} \right] \triangleq \text{VLB}, \quad (32) \end{aligned}$$

where $\stackrel{(a)}{\geq}$ comes from the Jensen inequality for the log function. In order to clarify the logical structure of the VLB,

¹VLB is also known as the evidence lower bound (ELBO) in some literature.

we further break down the VLB into its three constituent components by substituting (25) into (32) as

$$\begin{aligned} \text{VLB} &= -\mathbb{E}_{q(\mathbf{x}_i^{(0:T)})} \left[\underbrace{-\ln p_\theta(\mathbf{x}_i^{(0)} | \mathbf{x}_i^{(1)}, \hat{\mathbf{H}}_s)}_{L_1} \right. \\ &\quad \left. + \underbrace{D_{\text{KL}}(q(\mathbf{x}_i^{(T)} | \mathbf{x}_i^{(0)}) \| p(\mathbf{x}_i^{(T)}))}_{L_2} \right. \\ &\quad \left. + \underbrace{\sum_{t=2}^T D_{\text{KL}}(q(\mathbf{x}_i^{(t-1)} | \mathbf{x}_i^{(t)}, \mathbf{x}_i^{(0)}) \| p_\theta(\mathbf{x}_i^{(t-1)} | \mathbf{x}_i^{(t)}, \hat{\mathbf{H}}_s))}_{\text{diffusion loss}} \right], \quad (33) \end{aligned}$$

where $D_{\text{KL}}(\cdot \| \cdot)$ denotes the Kullback-Leibler (KL) divergence. Note that for a long time diffusion sequence with a relatively large T , L_1 is relatively small compared to the diffusion loss. Besides, L_2 is the KL divergence of two deterministic Gaussian distributions irrelevant to θ and is thus a constant. Therefore, we aim to minimize the diffusion loss that is the sum of a series of KL divergences. Since both $q(\mathbf{x}_i^{(t-1)} | \mathbf{x}_i^{(t)}, \mathbf{x}_i^{(0)})$ and $p_\theta(\mathbf{x}_i^{(t-1)} | \mathbf{x}_i^{(t)}, \hat{\mathbf{H}}_s)$ are Gaussian distributions according to (27) and (28), their KL divergence at time step t can be computed as

$$\begin{aligned} D_{\text{KL}}(q(\mathbf{x}_i^{(t-1)} | \mathbf{x}_i^{(t)}, \mathbf{x}_i^{(0)}) \| p_\theta(\mathbf{x}_i^{(t-1)} | \mathbf{x}_i^{(t)})) &= \frac{1}{2} \left[5 \frac{\gamma_t}{\beta_t} \right. \\ &\quad \left. + \frac{1}{\beta_t} \left\| \boldsymbol{\mu}_\theta(\mathbf{x}_i^{(t)}, t, \hat{\mathbf{H}}_s) - \boldsymbol{\mu}_t(\mathbf{x}_i^{(t)}, \mathbf{x}_i^{(0)}) \right\|_2^2 - 5 + 5 \ln \frac{\beta_t}{\gamma_t} \right] \\ &\stackrel{(a)}{=} \frac{1}{2} \left[5 \frac{1 - \bar{\alpha}_{t-1}}{1 - \bar{\alpha}_t} - 5 - 5 \ln \left(\frac{1 - \bar{\alpha}_{t-1}}{1 - \bar{\alpha}_t} \right) \right. \\ &\quad \left. + \frac{1}{\beta_t} \left\| \boldsymbol{\mu}_\theta(\mathbf{x}_i^{(t)}, t, \hat{\mathbf{H}}_s) - \frac{1}{\sqrt{\bar{\alpha}_t}} \left(\mathbf{x}_i^{(t)} - \frac{\beta_t}{\sqrt{1 - \bar{\alpha}_t}} \boldsymbol{\epsilon}_i^{(t)} \right) \right\|_2^2 \right], \quad (34) \end{aligned}$$

where $\stackrel{(a)}{=}$ is derived from (30) and (31). In order to maximize VLB, we aim to minimize the only variable $\left\| \boldsymbol{\mu}_\theta(\mathbf{x}_i^{(t)}, t, \hat{\mathbf{H}}_s) - \frac{1}{\sqrt{\bar{\alpha}_t}} \left(\mathbf{x}_i^{(t)} - \frac{\beta_t}{\sqrt{1 - \bar{\alpha}_t}} \boldsymbol{\epsilon}_i^{(t)} \right) \right\|_2^2$ in (34). Let $\boldsymbol{\epsilon}_\theta(\mathbf{x}_i^{(t)}, t, \hat{\mathbf{H}}_s)$ denote the reverse noise estimator for the normalized noise added to $\mathbf{x}_i^{(t-1)}$ in (31) during the forward diffusion process. Then, there is

$$\boldsymbol{\mu}_\theta(\mathbf{x}_i^{(t)}, t, \hat{\mathbf{H}}_s) = \frac{1}{\sqrt{\bar{\alpha}_t}} \left[\mathbf{x}_i^{(t)} - \frac{\beta_t}{\sqrt{1 - \bar{\alpha}_t}} \boldsymbol{\epsilon}_\theta(\mathbf{x}_i^{(t)}, t, \hat{\mathbf{H}}_s) \right]. \quad (35)$$

According to (35), minimizing $\left\| \boldsymbol{\mu}_\theta(\mathbf{x}_i^{(t)}, t, \hat{\mathbf{H}}_s) - \frac{1}{\sqrt{\bar{\alpha}_t}} \left(\mathbf{x}_i^{(t)} - \frac{\beta_t}{\sqrt{1 - \bar{\alpha}_t}} \boldsymbol{\epsilon}_i^{(t)} \right) \right\|_2^2$ is thereby equivalent to minimizing $\left\| \boldsymbol{\epsilon}_i^{(t)} - \boldsymbol{\epsilon}_\theta(\mathbf{x}_i^{(t)}, t, \hat{\mathbf{H}}_s) \right\|_2^2$. Since the reverse noise estimator is hard to formulate explicitly, we propose to model it as a neural network. To train this neural network, the loss function of the reverse noise estimator can

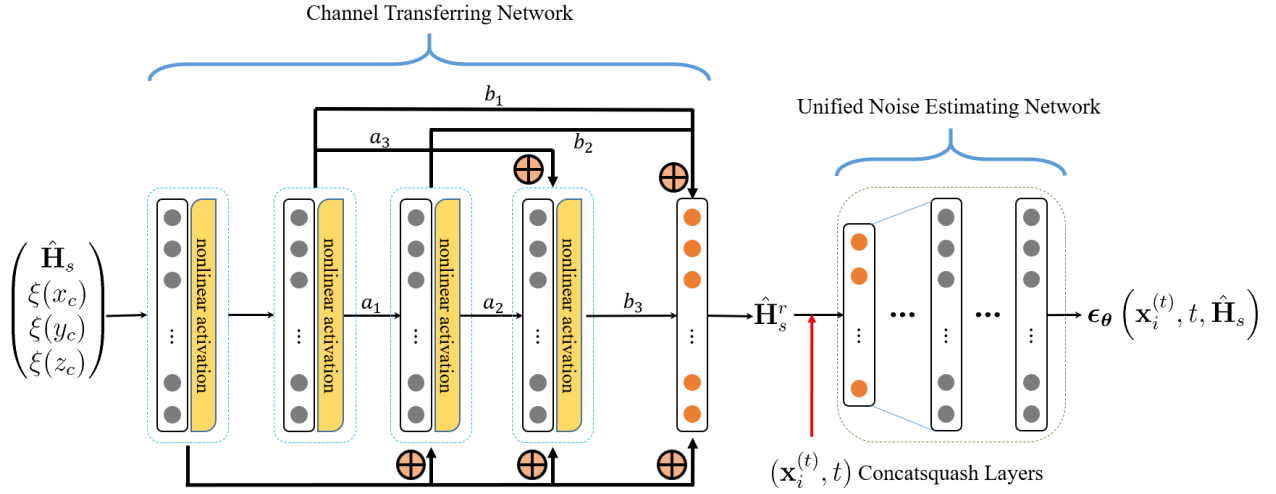


Fig. 3. Schematic diagram of the reverse noise estimator, which is composed of two cascaded neural networks: the channel transferring network and the unified noise estimating network.

be formulated by substituting (35) into (34) and dropping the constants, i.e.,

$$\begin{aligned} \text{Loss}_1 &= \mathbb{E}_{t, \mathbf{x}_i^{(0)}, \epsilon_i^{(t)} \sim \mathcal{N}(\mathbf{0}, \mathbf{I})} \left[\frac{\beta_t}{2\alpha_t(1 - \bar{\alpha}_t)} \right. \\ &\quad \left. \times \left\| \epsilon_i^{(t)} - \epsilon_\theta(\mathbf{x}_i^{(t)}, t, \hat{\mathbf{H}}_s) \right\|_2^2 \right] \\ &\stackrel{(a)}{\approx} \frac{1}{TN} \sum_{t=1}^T \sum_{i=1}^N \frac{\beta_t}{2\alpha_t(1 - \bar{\alpha}_t)} \left\| \epsilon_i^{(t)} - \epsilon_\theta(\mathbf{x}_i^{(t)}, t, \hat{\mathbf{H}}_s) \right\|_2^2, \end{aligned} \quad (36)$$

where $\stackrel{(a)}{\approx}$ approximates the loss function by the weighted mean squared error between the added noise and the estimated noise.

D. Reverse Noise Estimator

Since the sensing channel is influenced by not only the EM property but also the location of the target, training the reverse noise estimator is relatively easy when the target is situated at a predefined reference location. Define \mathbf{H}_s^r as the reference sensing channel when the target is translated to the reference location (x_r, y_r, z_r) with the shape, posture, and EM property unchanged. We will first transfer the sensing channel to the reference sensing channel and then estimate the noise in the diffusion process. The reverse noise estimator $\epsilon_\theta(\mathbf{x}_i^{(t)}, t, \hat{\mathbf{H}}_s)$ is composed of two cascaded neural networks: the channel transferring network and the unified noise estimating network, as shown in Fig. 3.

The channel transferring network plays the role of estimating the reference sensing channel \mathbf{H}_s^r by taking $\hat{\mathbf{H}}_s$ and (x_c, y_c, z_c) as the inputs. Despite the fact that neural networks can be universal function approximators, we found that having the channel transferring network directly operate on the input coordinates (x_c, y_c, z_c) leads to relatively poor representation of the fine-grained spatial variations in location. This is consistent with recent work by [33], which shows that the deep neural networks are biased towards learning

lower-frequency functions. However, by mapping the inputs to a higher-dimensional space with high-frequency sinusoidal functions prior to their entry into the channel transferring network, it becomes possible to achieve a more accurate fit of data with complex spatial intricacies [34].

Define the positional encoding function $\xi(\cdot)$ as a mapping from \mathbb{R} into a higher-dimensional space $\mathbb{R}^{(2L+1) \times 1}$. Then we apply $\xi(\cdot)$ separately to each of the three coordinate values as $[\xi(x_c), \xi(y_c), \xi(z_c)]$. The positional encoding function can be defined as

$$\begin{aligned} \xi(p) &= [p, \sin(2^0 \pi p), \cos(2^0 \pi p), \dots, \\ &\quad \sin(2^{L-1} \pi p), \cos(2^{L-1} \pi p)]^\top, p \in \{x_c, y_c, z_c\}. \end{aligned} \quad (37)$$

The channel transferring network takes $\xi(x_c), \xi(y_c), \xi(z_c)$, and $\hat{\mathbf{H}}_s$ as the inputs that are concatenated into a real-valued vector $[\text{vec}(\Re(\hat{\mathbf{H}}_s))^\top, \text{vec}(\Im(\hat{\mathbf{H}}_s))^\top, \xi(x_c)^\top, \xi(y_c)^\top, \xi(z_c)^\top]^\top$ for further processing. The reference sensing channel is estimated by the regular Neural ODE [35], [36] with DenseNet structure [37]. We set the dimensions of all the hidden layers as 512. The parameters $(a_1, a_2, a_3, b_1, b_2, b_3)$ in Fig. 3 denote the trainable coefficients multiplied to the output of the previous layer.

In order to train the channel transferring network, we define the loss function as the normalized mean square error (NMSE) of the reference sensing channel estimation, i.e.,

$$\text{Loss}_2 = \text{NMSE}(\hat{\mathbf{H}}_s^r) = \frac{\left\| \mathbf{H}_s^r - \hat{\mathbf{H}}_s^r \right\|_F^2}{\left\| \mathbf{H}_s^r \right\|_F^2}. \quad (38)$$

As the second part of the reverse noise estimator, the unified noise estimating network is composed of a series of L_{cs} concatsquash layers [38] defined as

$$\mathbf{e}^{n+1} = (\mathbf{W}_1^n \mathbf{e}^n + \mathbf{b}_1^n) \odot \text{Sigmoid}(\mathbf{W}_2^n \mathbf{e}^n + \mathbf{b}_2^n) + \mathbf{W}_3^n \mathbf{e}^n, \quad (39)$$

where \mathbf{e}^n is the input to the n -th layer and \mathbf{e}^{n+1} is the output. The input to the first layer is the 5D

Algorithm 2 Training Reverse Noise Estimator

```

1: repeat
2:   Sample  $\mathcal{X}^{(0)} \sim q(\mathcal{X}^{(0)})$ 
3:   Select the reference sensing channel  $\mathbf{H}_s^r$  corresponding
     to  $\mathcal{X}^{(0)}$ 
4:   for  $t = 1, \dots, T$  do
5:     for  $i = 1, \dots, N$  do
6:       Sample  $\epsilon_i^{(t)} \sim \mathcal{N}(\mathbf{0}, \mathbf{I})$ 
7:       Compute  $\mathbf{x}_i^{(t)} \sim q(\mathbf{x}_i^{(t)} | \mathbf{x}_i^{(0)})$ 
8:     end for
9:   end for
10:  Compute  $\text{Loss}_1$  according to (36)
11:  Compute  $\nabla \text{Loss}_1$ , and perform gradient descent.
12: until converged
13: repeat
14:  Sample  $\mathcal{X}^{(0)} \sim q(\mathcal{X}^{(0)})$  and sample  $(x_c, y_c, z_c)$ 
     uniformly and randomly in the sensing area
15:  Select  $\mathbf{H}_s$  and  $\mathbf{H}_s^r$  corresponding to  $\mathcal{X}^{(0)}$  and
      $(x_c, y_c, z_c)$ 
16:  Compute  $\hat{\mathbf{H}}_s^r$  and compute  $\text{Loss}_2$  according to (38)
17:  Compute  $\nabla \text{Loss}_2$ , and perform gradient descent.
18: until converged
  
```

point $\mathbf{x}_i^{(t)}$, and the output of the last layer is the estimated noise $\epsilon_\theta(\mathbf{x}_i^{(t)}, t, \hat{\mathbf{H}}_s)$. Moreover, we define the real-valued concatenated context vector as $\mathbf{c} \triangleq \left[t, \sin(t), \cos(t), \sin(2t), \cos(2t), \text{vec}(\Re(\hat{\mathbf{H}}_s^r))^\top, \text{vec}(\Im(\hat{\mathbf{H}}_s^r))^\top \right]^\top$. The context vector incorporates the embedded random Fourier features of the time step t [39] and the estimated reference sensing channel matrix $\hat{\mathbf{H}}_s^r$. Besides, $\{\mathbf{W}_1^n, \mathbf{W}_2^n, \mathbf{W}_3^n, \mathbf{b}_1^n, \mathbf{b}_2^n\}_{n=1:10}$ are trainable weights and biases in the neural network. We use the Swish activation function to create non-linearity between the layers [40].

In the training procedure, we first train the unified noise estimating network with Loss_1 and then train the channel transferring network with Loss_2 , where we assume the center of the target is sampled from a predetermined sensing area. Since the two loss functions are irrelevant to each other, the two networks are trained independently. With the loss function (36) and (38), the procedure to train the reverse noise estimator $\epsilon_\theta(\mathbf{x}_i^{(t)}, t, \hat{\mathbf{H}}_s)$ is summarized in Algorithm 2.

V. BEAMFORMING DESIGN WITH TRADEOFF BETWEEN SENSING AND COMMUNICATIONS

Since it is relatively hard to directly minimize the Chamfer distance between the reconstructed 5D point cloud and the ground truth through the beamforming design, we aim to minimize the CRB of sensing channel estimation in (9) alternatively, which is positively related to the discrepancy of 5D point cloud reconstruction. In particular, we would optimize the transmit covariance matrix \mathbf{S}_x to minimize the CRB of sensing channel estimation, while guaranteeing the minimum communications rate \bar{R} for each UE, and subject to the maximum transmit power constraint P . Specifically, the

communications achievable rate-constrained CRB minimization problem is formulated as

$$(P1) : \min_{\mathbf{S}_x, \mathbf{R}_k, k=1, \dots, K} \text{tr}(\text{CRB}) = \frac{N_r \sigma_s^2}{L} \text{tr}(\mathbf{S}_x^{-1}) \quad (40a)$$

$$\text{s.t.} \min_k \log_2 \left(1 + \frac{\mathbf{h}_k^H \mathbf{R}_k \mathbf{h}_k}{\sigma_k^2 + \mathbf{h}_k^H (\mathbf{S}_x - \mathbf{R}_k) \mathbf{h}_k} \right) \geq \bar{R}, \quad (40b)$$

$$\text{tr}(\mathbf{S}_x) \leq P, \quad (40c)$$

$$\mathbf{S}_x \succeq \mathbf{0}, \quad \mathbf{R}_k \succeq \mathbf{0}, \quad k = 1, \dots, K, \quad (40d)$$

$$\text{rank}(\mathbf{R}_k) = 1, \quad k = 1, \dots, K, \quad (40e)$$

$$\mathbf{R} - \sum_{k=1}^K \mathbf{R}_k \succeq \mathbf{0}, \quad k = 1, \dots, K. \quad (40f)$$

By introducing $\Gamma = \frac{1}{2^{\bar{R}} - 1}$, problem (P1) can be equivalently reformulated as

$$(P2) : \min_{\mathbf{S}_x, \mathbf{R}_k, k=1, \dots, K} \text{tr}(\mathbf{S}_x^{-1}) \quad (41a)$$

$$\text{s.t.} \quad (1 + \Gamma) \mathbf{h}_k^H \mathbf{R}_k \mathbf{h}_k \geq \sigma_k^2 + \mathbf{h}_k^H \mathbf{S}_x \mathbf{h}_k, \quad k = 1, \dots, K, \quad (41b)$$

$$\text{tr}(\mathbf{S}_x) \leq P, \quad (41c)$$

$$\mathbf{S}_x \succeq \mathbf{0}, \quad \mathbf{R}_k \succeq \mathbf{0}, \quad k = 1, \dots, K, \quad (41d)$$

$$\text{rank}(\mathbf{R}_k) = 1, \quad k = 1, \dots, K, \quad (41e)$$

$$\mathbf{S}_x - \sum_{k=1}^K \mathbf{R}_k \succeq \mathbf{0}, \quad k = 1, \dots, K. \quad (41f)$$

By dropping the rank-one constraints (41e), (P2) becomes a convex optimization problem and can be solved via CVX efficiently [41]. Denote $\tilde{\mathbf{S}}_x$ and $\tilde{\mathbf{R}}_k$ as the feasible solutions to problem (P2) without the rank-one constraints (41e), which are referred to as the semidefinite relaxation (SDR) solutions [42]. We can then construct the suboptimal communications beamforming matrix $\tilde{\mathbf{W}}_c = [\hat{\mathbf{w}}_{c,1}, \hat{\mathbf{w}}_{c,2}, \dots, \hat{\mathbf{w}}_{c,K}]$ and $\hat{\mathbf{R}}_k$ from the SDR solutions as

$$\hat{\mathbf{w}}_{c,k} = \frac{\tilde{\mathbf{R}}_k \mathbf{h}_k}{\sqrt{\mathbf{h}_k^H \tilde{\mathbf{R}}_k \mathbf{h}_k}}, \quad \hat{\mathbf{R}}_k = \hat{\mathbf{w}}_{c,k} \hat{\mathbf{w}}_{c,k}^H, \quad k = 1, \dots, K. \quad (42)$$

Given $\tilde{\mathbf{S}}_x$ and $\hat{\mathbf{R}}_k$, the suboptimal sensing beamforming matrix $\hat{\mathbf{W}}_s = [\hat{\mathbf{w}}_{s,1}, \hat{\mathbf{w}}_{s,2}, \dots, \hat{\mathbf{w}}_{s,N_t}]$ can be constructed from the SDR solutions using the Cholesky decomposition of the sensing Gram matrix as

$$\hat{\mathbf{W}}_s \hat{\mathbf{W}}_s^H = \hat{\mathbf{R}}_s = \tilde{\mathbf{S}}_x - \sum_{k=1}^K \hat{\mathbf{R}}_k. \quad (43)$$

Different from most literature using SDR, we need to prove that $\tilde{\mathbf{S}}_x$ and $\tilde{\mathbf{R}}_k$ satisfy constraints (41b)-(41f) to ensure they are feasible solutions to problem (P2). It can be easily seen that constraints (41c)-(41e) hold obviously with (42) and (43). Therefore, we only need to check the remaining constraints (41b) and (41f).

Constraint (41b) holds with $\hat{\mathbf{R}}_k$, because there is $\mathbf{h}_k^H \hat{\mathbf{R}}_k \mathbf{h}_k = \mathbf{h}_k^H \tilde{\mathbf{R}}_k \mathbf{h}_k$ and (41b) holds with $\tilde{\mathbf{R}}_k$. In order to check constraint (41f), we only need to prove that

$\tilde{\mathbf{R}}_k - \hat{\mathbf{R}}_k \succeq 0$. Based on the Cauchy-Schwarz inequality, for any $\mathbf{u} \in \mathbb{C}^{N_t \times 1}$, there is

$$\left(\mathbf{h}_k^H \tilde{\mathbf{R}}_k \mathbf{h}_k \right) \left(\mathbf{u}^H \tilde{\mathbf{R}}_k \mathbf{u} \right) = \left\| \tilde{\mathbf{R}}_k^{\frac{1}{2}} \mathbf{h}_k \right\|_2^2 \left\| \tilde{\mathbf{R}}_k^{\frac{1}{2}} \mathbf{u} \right\|_2^2 \geq \left| \mathbf{u}^H \tilde{\mathbf{R}}_k \mathbf{h}_k \right|^2, \quad (44)$$

where $\tilde{\mathbf{R}}_k^{\frac{1}{2}}$ is the Cholesky decomposition of $\tilde{\mathbf{R}}_k$ that satisfies $(\tilde{\mathbf{R}}_k^{\frac{1}{2}})^H \tilde{\mathbf{R}}_k^{\frac{1}{2}} = \tilde{\mathbf{R}}_k$. Substituting (42) into $\tilde{\mathbf{R}}_k$ and then utilizing (44), we have

$$\mathbf{u}^H \left(\tilde{\mathbf{R}}_k - \hat{\mathbf{R}}_k \right) \mathbf{u} = \mathbf{u}^H \tilde{\mathbf{R}}_k \mathbf{u} - \frac{\left| \mathbf{u}^H \tilde{\mathbf{R}}_k \mathbf{h}_k \right|^2}{\mathbf{h}_k^H \tilde{\mathbf{R}}_k \mathbf{h}_k} \geq 0. \quad (45)$$

Due to the arbitrariness of $\mathbf{u} \in \mathbb{C}^{N_t \times 1}$ in (45), there is $\tilde{\mathbf{R}}_k - \hat{\mathbf{R}}_k \succeq 0$. Since there is $\tilde{\mathbf{S}}_x - \sum_{k=1}^K \tilde{\mathbf{R}}_k \succeq 0$, we have

$$\tilde{\mathbf{S}}_x - \sum_{k=1}^K \hat{\mathbf{R}}_k = \tilde{\mathbf{S}}_x - \sum_{k=1}^K \tilde{\mathbf{R}}_k + \sum_{k=1}^K \left(\tilde{\mathbf{R}}_k - \hat{\mathbf{R}}_k \right) \succeq 0. \quad (46)$$

Therefore, we have proven that $\tilde{\mathbf{S}}_x$ and $\hat{\mathbf{R}}_k$ are feasible solutions to problem (P2).

VI. SIMULATION RESULTS AND ANALYSIS

Suppose the largest possible target can be contained within a cubic region D whose size is $1 \text{ m} \times 1 \text{ m} \times 1 \text{ m}$. We choose the number of scatter points that constitute the target as $N = 2048$. Assume the BS is located at $(0, 0, 0) \text{ m}$ and is responsible for sensing the target within the range of a 30 m radius sector on the horizontal plane, denoted by $S = \{(x, y, 0) \mid \arctan \frac{y}{x} \in [-60^\circ, 60^\circ], \sqrt{x^2 + y^2} \leq 30 \text{ m}\}$. The BS is equipped with a uniform linear array (ULA) with $N_t = 64$ transmitting antennas and a ULA with $N_r = 64$ receiving antennas. The transmitting and the receiving ULAs are both centered at $(0, 0, 0) \text{ m}$ and are parallel to y and z directions, respectively, which is analogous to the Mills-Cross configuration [43]. The transmitting and the receiving antennas are set as dipoles polarized along z and y directions, respectively. The carrier frequency is set as $f = 2.99 \text{ GHz}$ and the corresponding wavelength is $\lambda = 0.1 \text{ m}$. The inter-antenna spacing for both the transmitting and the receiving ULAs is set as $\lambda/2 = 0.05 \text{ m}$. We assume the system operates with a bandwidth of $B = 10 \text{ MHz}$, and then all the thermal noise powers are set as $\sigma_s^2 = \sigma_k^2 = -174 + 10 \log_{10} B = -104 \text{ dBm}$, $k = 1, \dots, K$. A total of $L = 160$ ISAC symbols are transmitted. Besides, the communications channel \mathbf{h}_k is generated as i.i.d. CSCG variables $\mathcal{CN}(\mathbf{0}, p_l \mathbf{I}_{N_t})$ for all k . The pathloss p_l is set as $p_l = \frac{G_t G_r \lambda^2}{(4\pi d)^2}$, where G_t and G_r are both set as 3 dBi, and d is uniformly and randomly sampled from $[50, 150] \text{ m}$.

For the diffusion model, we set the number of time steps as $T = 200$, and the diffusion coefficients β_t linearly increase from $\beta_1 = 0.0001$ to $\beta_T = 0.05$. In the reverse noise estimator, we set $\bar{L} = 10$ and $L_{cs} = 10$. The dimensions of the 10 concatsquash layers are set as 5-16-64-128-256-512-256-128-64-16-5, respectively. In order to train the reverse noise estimator, we generate 100000 targets from the ShapeNet dataset [44], which are uniformly and randomly located within the sector S . The reference location in the channel transferring

network is set as $(x_r, y_r, z_r) = (3, 0, 0) \text{ m}$. The dataset is then split into training, testing, and validation sets by the ratio 80%, 10%, and 10%, respectively. During the training process, we use the Adam optimizer and set the batch size as 256. Besides, we use the ground truth values of the sensing channel and the reference sensing channel for training. In order to compute the forward scattering, equation (14) is first converted into a discrete form by the methods of moments (MoM), and then the unknown total electric field $\mathbf{E}^t(\mathbf{r})$ is determined using the stabilized biconjugate gradient fast Fourier transform (BCGS-FFT) technique [45].

Moreover, we introduce the mean Chamfer distance (MCD) between the ground truth and the estimated point clouds as the criterion to quantitatively evaluate the performance of EM property sensing, defined as

$$\text{MCD} = 10 \log_{10} \left[\frac{1}{|\mathcal{T}|} \sum_{\mathcal{X}^{(0)} \in \mathcal{T}} \left(\frac{1}{N} \sum_{\mathbf{x} \in \mathcal{X}^{(0)}} \min_{\mathbf{y} \in \hat{\mathcal{X}}^{(0)}} \|\mathbf{x} - \mathbf{y}\|_2^2 + \frac{1}{N} \sum_{\mathbf{y} \in \hat{\mathcal{X}}^{(0)}} \min_{\mathbf{x} \in \mathcal{X}^{(0)}} \|\mathbf{x} - \mathbf{y}\|_2^2 \right) \right], \quad (47)$$

where \mathcal{T} denotes the test dataset, and $|\mathcal{T}|$ denotes the number of samples in the test dataset.

A. EM Property Sensing Performance versus P

To illustrate the EM property sensing results vividly, we present the reconstructed point clouds of the target based on relative permittivity and conductivity, respectively, with $K = 2$ and $\bar{R} = 5 \text{ bps/Hz}$ in Fig. 4. The center of the target is at $(15, 0, 0) \text{ m}$, and the target is shown in the coordinate system relative to its center. It is seen from Fig. 4 that, the reconstructed point clouds can reflect the general shape of the target. The values of EM property reconstructed with $P = 15 \text{ dBm}$ is much more accurate compared to those reconstructed with $P = 7 \text{ dBm}$. Moreover, a higher P value results in a more accurate reconstructed shape of the target.

We explore the MCD of the reconstructed 5D point clouds versus P in Fig. 5. We set $\bar{R} = 5 \text{ bps/Hz}$, and the center of the target is at $(15, 0, 0) \text{ m}$. It is seen from Fig. 5 that, the MCD decreases with the increase of P in all cases, and the MCD is larger when K is larger. As more UEs need to be served, the power allocated to the sensing service is smaller, which leads to a larger error of the sensing channel estimation and a larger MCD of the 5D point cloud reconstruction. The MCD decreases fast in the beginning when P increases from 5 dBm to 9 dBm. When P reaches a threshold of approximately 10 dBm, the MCD reduces almost linearly in dB values with respect to P . When P is relatively large, the discrepancy among different K is not significant, which indicates that the transmit power can be mainly allocated to the EM property sensing service, and communications achievable rate limitations play a relatively small role in this period.

B. EM Property Sensing Performance versus \bar{R}

To demonstrate the EM property sensing results, we present images of the target reconstructed based on relative

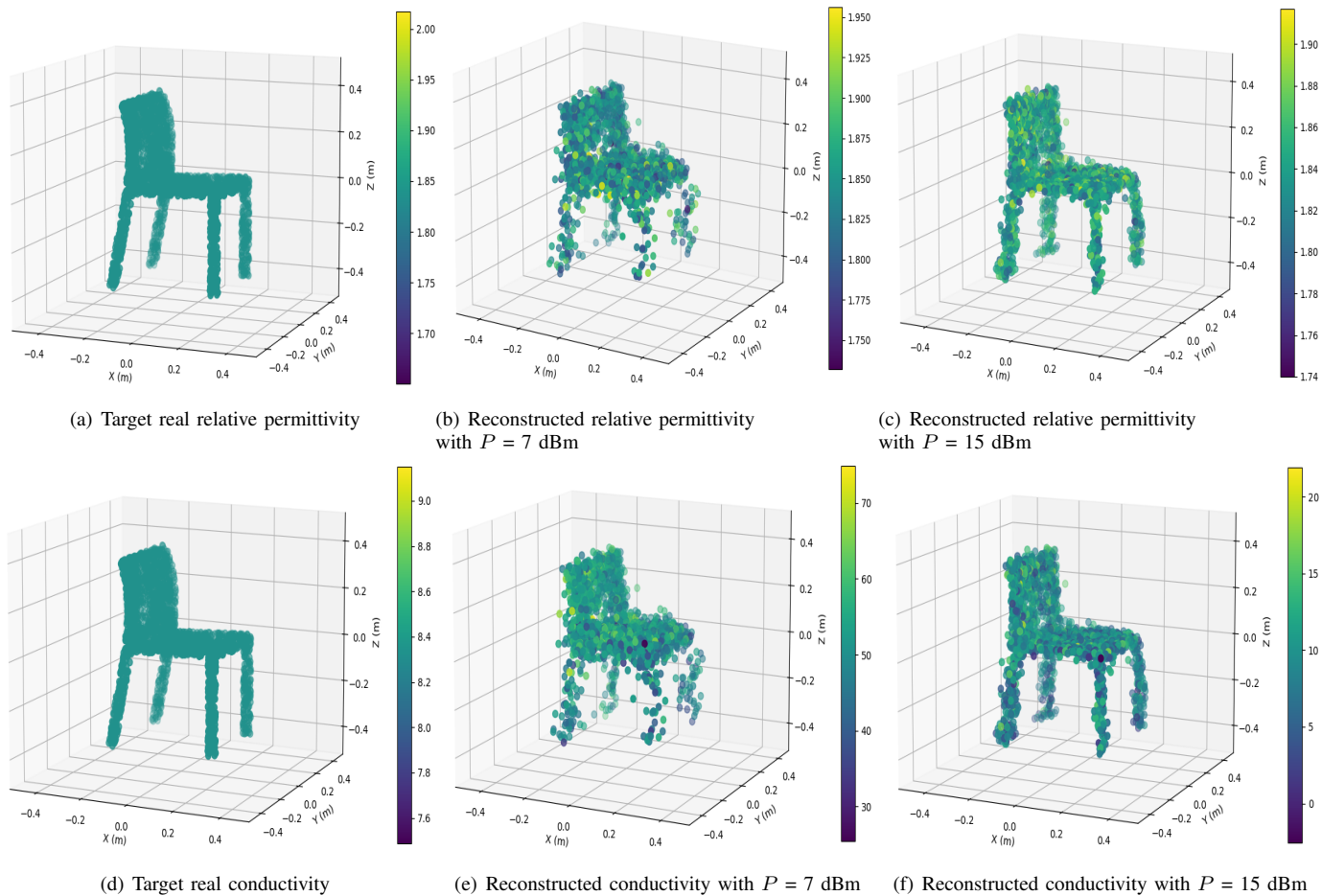


Fig. 4. EM property sensing results versus P with $K = 2$ and $\bar{R} = 5$ bps/Hz. The center of the target is at $(15, 0, 0)$ m. The target is shown in the coordinate system relative to its center. Unit of conductivity is mS/m.

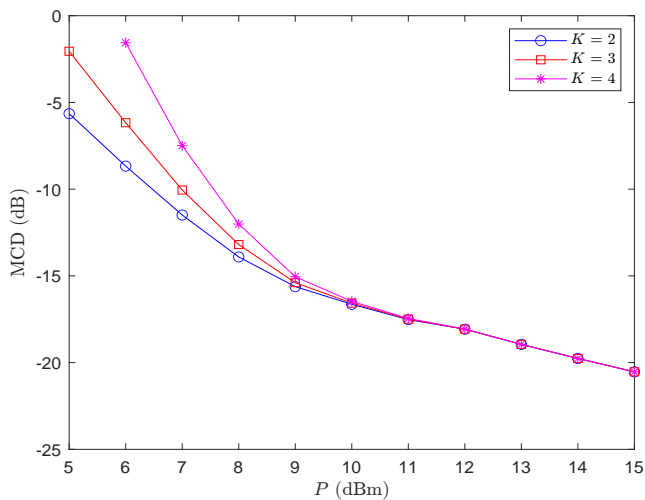


Fig. 5. MCD of 5D point clouds versus P with $\bar{R} = 5$ bps/Hz. The center of the target is at $(15, 0, 0)$ m.

permittivity and conductivity with $K = 2$ and $P = 15$ dBm. The center of the target is at $(15, 0, 0)$ m. As shown in Fig. 6, the shape of the target reconstructed with $\bar{R} = 4$ bps/Hz is more accurate compared to that reconstructed with

$\bar{R} = 6$ bps/Hz. Moreover, a smaller \bar{R} yields more accurate reconstructed values of relative permittivity and conductivity.

We investigate the MCD of the reconstructed 5D point clouds versus \bar{R} with $P = 15$ dBm in Fig. 7. The three lines are also known as the Pareto boundary of the MCD-rate region for different k . It is seen that, MCD increases with the increase of \bar{R} in all cases, and the MCD is smaller with fewer communications UEs. When \bar{R} is relatively low, the discrepancy among different K is not pronounced, which indicates that the transmit power is mainly allocated to the EM property sensing service, and communications achievable rate limitations play a relatively small role in this period. When \bar{R} increases to a certain threshold, the minimum achievable rate can not be satisfied even when all transmit power is allocated to the communications service, which makes the feasible solution to problem (P1) nonexistent. When the number of UEs increases, the maximum feasible \bar{R} decreases, because less power is allocated to the EM property sensing service.

C. EM Property Sensing Performance versus Location of the Target

To illustrate the EM property sensing results vividly, we present the reconstructed point clouds of the target based on relative permittivity and conductivity, respectively, with

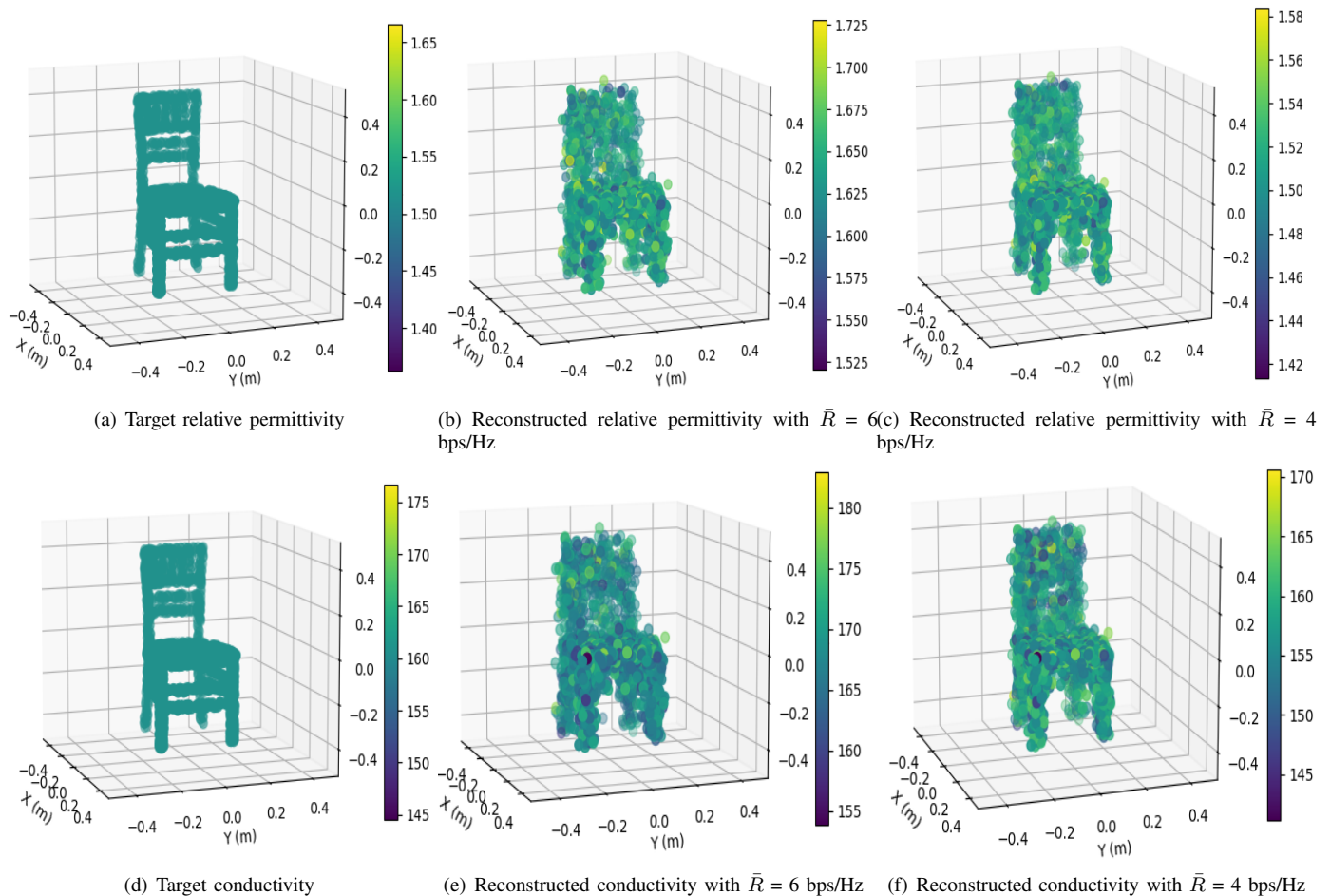


Fig. 6. EM property sensing results versus \bar{R} with $K = 2$ and $P = 15$ dBm. The center of the target is at $(15, 0, 0)$ m. The target is shown in the coordinate system relative to its center. Unit of conductivity is mS/m.

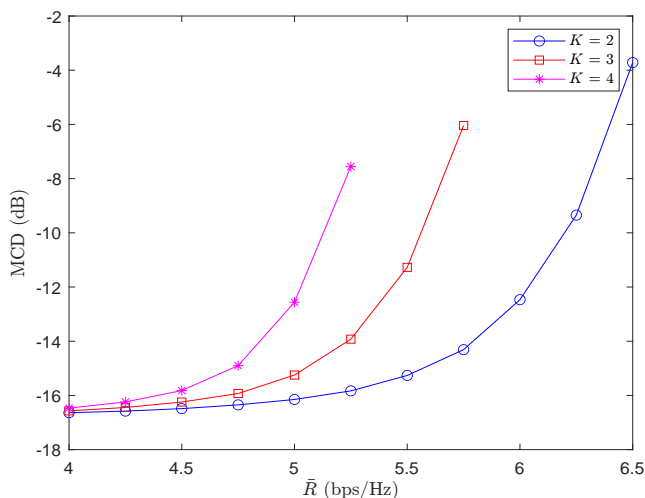


Fig. 7. MCD of 5D point clouds versus \bar{R} with $P = 15$ dBm. The center of the target is at $(15, 0, 0)$ m.

$P = 15$ dBm, $\bar{R} = 4$ bps/Hz, and $K = 2$ in Fig. 8. The target is shown in the coordinate system relative to its center. It is seen from Fig. 8 that, the reconstructed 5D point clouds can reflect the general shape of the target. The values

of EM property reconstructed with target at $(5, 0, 0)$ m is more accurate compared to those reconstructed with target at $(25, 0, 0)$ m. Moreover, a closer distance results in a more accurate reconstructed shape of the target.

We explore the MCD of the reconstructed 5D point clouds versus the location of the target in Fig. 9. We set $P = 15$ dBm, $\bar{R} = 4$ bps/Hz, and $K = 2$. It is seen from Fig. 9 that, the MCD is generally smaller when the target is in closer proximity to the BS. This is because when the target is closer to the BS, the sensing channel has more effective degrees of freedom (EDoF) [46] and more diverse spatial features of the estimated sensing channel can be extracted by the channel transferring network. Besides, when the target is closer to the BS, the power of the echo signals becomes larger, which results in a larger sensing SNR. Thus, the NMSE of the reference sensing channel estimation is smaller, and the MCD of 5D point cloud reconstruction is smaller accordingly. The MCD does not vary significantly with the change of the angle, which indicates that the proposed method can sense the EM property of the target effectively in any direction of the sector S .

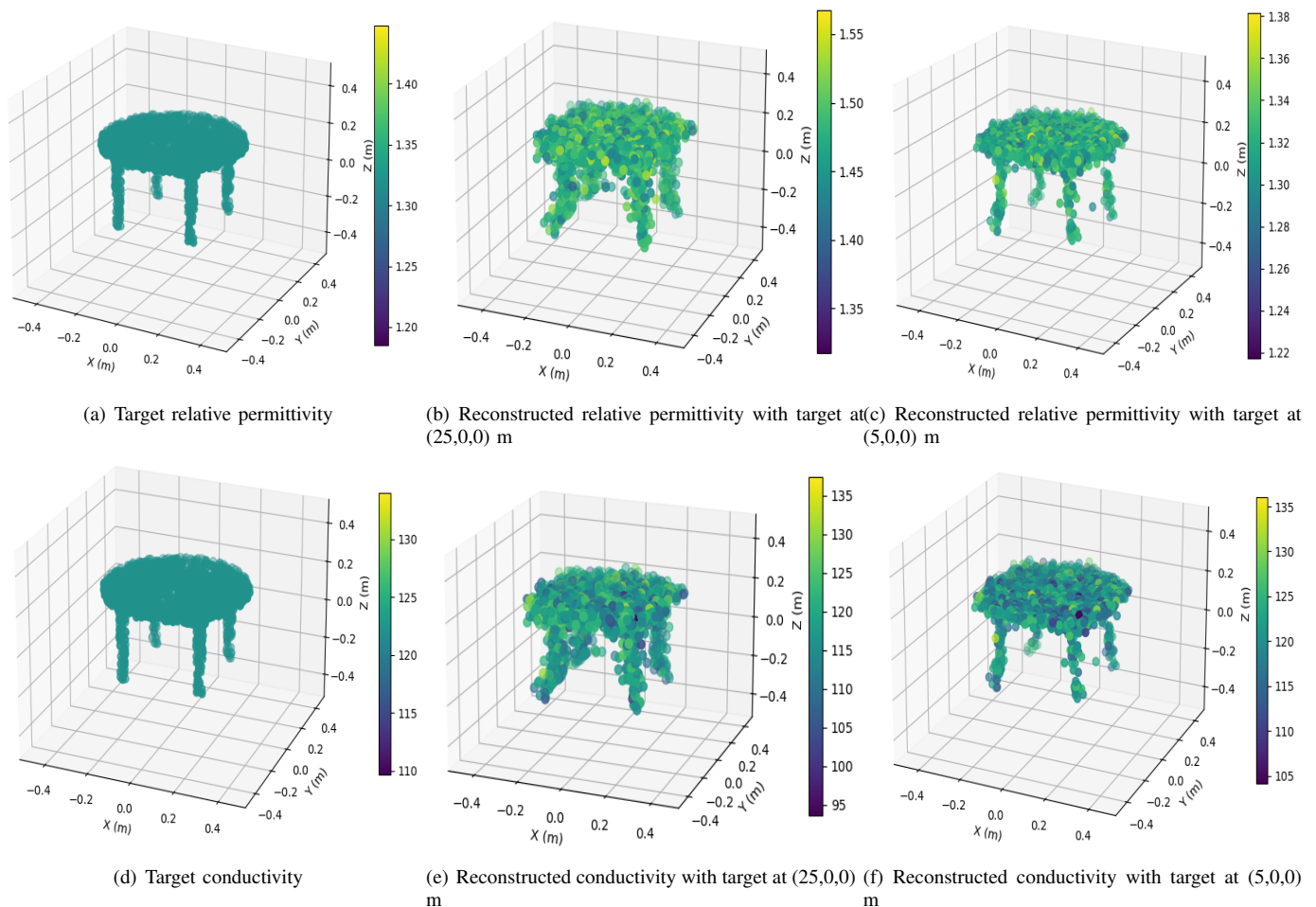


Fig. 8. EM property sensing results versus location with $P = 15$ dBm, $\bar{R} = 4$ bps/Hz, and $K = 2$. The target is shown in the coordinate system relative to its center. Unit of conductivity is mS/m.

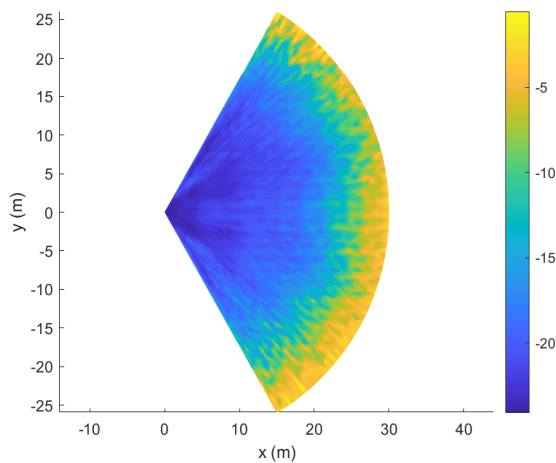


Fig. 9. MCD of 5D point clouds versus location with $P = 15$ dBm, $\bar{R} = 4$ bps/Hz, and $K = 2$.

VII. CONCLUSION

In this paper, we propose a groundbreaking ISAC scheme that harnesses the power of the diffusion model to precisely

capture the EM property of a target within a predetermined sensing area. The innovative approach begins with the estimation of the sensing channel using both communications and sensing signals. Subsequently, the diffusion model is applied to create a comprehensive point cloud, offering a vivid 3D depiction of the target's EM property distribution, encompassing essential attributes such as shape, relative permittivity, and conductivity. We further emphasize the importance of high-fidelity reconstruction by designing communications and sensing beamforming matrices that aim to minimize the MCD between the actual and the estimated point clouds. This optimization is meticulously conducted under the constraints of maximum transmit power and a minimum communications rate for UE. The simulation results demonstrate the effectiveness of the proposed method to realize high-quality reconstruction of the target's EM property. Moreover, the method's robustness in sensing the EM property of the target, regardless of its position within the sensing area, demonstrates its versatility and potential for various practical applications requiring accurate EM property sensing. The proposed ISAC scheme stands as a significant advancement in the field of wireless communications and sensing, paving the way for more precise and reliable EM property assessments.

REFERENCES

- [1] Q. Zhang, H. Sun, X. Gao, X. Wang, and Z. Feng, "Time-division ISAC enabled connected automated vehicles cooperation algorithm design and performance evaluation," *IEEE J. Sel. Areas Commun.*, vol. 40, no. 7, pp. 2206–2218, 2022.
- [2] H. Luo, T. Zhang, C. Zhao, Y. Wang, B. Lin, Y. Jiang, D. Luo, and F. Gao, "Integrated sensing and communications framework for 6g networks," *arXiv preprint arXiv:2405.19925*, 2024.
- [3] Z. Ren, Y. Peng, X. Song, Y. Fang, L. Qiu, L. Liu, D. W. K. Ng, and J. Xu, "Fundamental CRB-rate tradeoff in multi-antenna ISAC systems with information multicasting and multi-target sensing," *IEEE Trans. Wireless Commun.*, 2023.
- [4] Y. Jiang, F. Gao, Y. Liu, S. Jin, and T. J. Cui, "Near-field computational imaging with RIS generated virtual masks," *IEEE Trans. Antennas Propag.*, vol. 72, no. 5, pp. 4383–4398, Apr. 2024.
- [5] F. Dong, F. Liu, Y. Cui, W. Wang, K. Han, and Z. Wang, "Sensing as a service in 6G perceptive networks: A unified framework for ISAC resource allocation," *IEEE Trans. Wireless Commun.*, 2022.
- [6] Y. Jiang, F. Gao, M. Jian, S. Zhang, and W. Zhang, "Reconfigurable intelligent surface for near field communications: Beamforming and sensing," *IEEE Trans. Wireless Commun.*, vol. 22, no. 5, pp. 3447–3459, 2023.
- [7] Y. Zhong, T. Bi, J. Wang, J. Zeng, Y. Huang, T. Jiang, Q. Wu, and S. Wu, "Empowering the v2x network by integrated sensing and communications: Background, design, advances, and opportunities," *IEEE Network*, vol. 36, no. 4, pp. 54–60, 2022.
- [8] T. Ma, Y. Xiao, X. Lei, and M. Xiao, "Integrated sensing and communication for wireless extended reality (xr) with reconfigurable intelligent surface," *IEEE J. Sel. Signal Process.*, 2023.
- [9] Y. Cui, F. Liu, X. Jing, and J. Mu, "Integrating sensing and communications for ubiquitous IoT: Applications, trends, and challenges," *IEEE Network*, vol. 35, no. 5, pp. 158–167, 2021.
- [10] A. Alkhateeb, S. Jiang, and G. Charan, "Real-time digital twins: Vision and research directions for 6G and beyond," *IEEE Communications Magazine*, 2023.
- [11] P. Gao, L. Lian, and J. Yu, "Cooperative ISAC with direct localization and rate-splitting multiple access communication: A Pareto optimization framework," *IEEE J. Sel. Areas Commun.*, vol. 41, no. 5, pp. 1496–1515, 2023.
- [12] X. Meng, F. Liu, C. Masouros, W. Yuan, Q. Zhang, and Z. Feng, "Vehicular connectivity on complex trajectories: Roadway-geometry aware ISAC beam-tracking," *IEEE Trans. Wireless Commun.*, 2023.
- [13] Y. Tao and Z. Zhang, "Distributed computational imaging with reconfigurable intelligent surface," in *2020 International Conference on Wireless Communications and Signal Processing (WCSP)*, pp. 448–454, Oct. 2020.
- [14] Y. Jiang, F. Gao, and S. Jin, "Electromagnetic property sensing: A new paradigm of integrated sensing and communication," *IEEE Trans. Wireless Commun.*, 2024, May.
- [15] Y. Jiang, F. Gao, S. Jin, and T. J. Cui, "Electromagnetic property sensing in ISAC with multiple base stations: Algorithm, pilot design, and performance analysis," *arXiv preprint arXiv:2405.06364*, 2024.
- [16] Z. Zhu, M. Gong, G. Sun, M. De, F. Liu, and Y. Liu, "AI-enabled star-ris aided mimo isac secure communications," *arXiv preprint arXiv:2402.16413*, 2024.
- [17] G. Zhu, Z. Lyu, X. Jiao, P. Liu, M. Chen, J. Xu, S. Cui, and P. Zhang, "Pushing ai to wireless network edge: An overview on integrated sensing, communication, and computation towards 6g," *Science China Information Sciences*, vol. 66, no. 3, p. 130301, 2023.
- [18] D. Wen, P. Liu, G. Zhu, Y. Shi, J. Xu, Y. C. Eldar, and S. Cui, "Task-oriented sensing, computation, and communication integration for multi-device edge ai," *IEEE Transactions on Wireless Communications*, 2023.
- [19] J. Wang, H. Du, D. Niyato, J. Kang, S. Cui, X. Shen, and P. Zhang, "Generative ai for integrated sensing and communication: Insights from the physical layer perspective," *arXiv preprint arXiv:2310.01036*, 2023.
- [20] L. Li, L. G. Wang, F. L. Teixeira, C. Liu, A. Nehorai, and T. J. Cui, "Deepnis: Deep neural network for nonlinear electromagnetic inverse scattering," *IEEE Trans. Antennas Propag.*, vol. 67, no. 3, pp. 1819–1825, 2018.
- [21] H. Zhang, Y. Chen, T. J. Cui, F. L. Teixeira, and L. Li, "Probabilistic deep learning solutions to electromagnetic inverse scattering problems using conditional renormalization group flow," *IEEE Trans. Microwave Theory Tech.*, vol. 70, no. 11, pp. 4955–4965, 2022.
- [22] S. H. Chan, "Tutorial on diffusion models for imaging and vision," *arXiv preprint arXiv:2403.18103*, 2024.
- [23] D. Kingma, T. Salimans, B. Poole, and J. Ho, "Variational diffusion models," *Advances in neural information processing systems*, vol. 34, pp. 21696–21707, 2021.
- [24] S. M. Kay, *Fundamentals of Statistical Signal Processing: Estimation Theory*. Prentice-Hall, Inc., 1993.
- [25] Z. Liu and Z. Nie, "Subspace-based variational Born iterative method for solving inverse scattering problems," *IEEE Geosci. Remote Sens. Lett.*, vol. 16, no. 7, pp. 1017–1020, 2019.
- [26] J. Guillemoteau, P. Sailhac, and M. Behaegel, "Fast approximate 2D inversion of airborne tem data: Born approximation and empirical approach," *Geophysics*, vol. 77, no. 4, pp. WB89–WB97, 2012.
- [27] O. J. F. Martin and N. B. Piller, "Electromagnetic scattering in polarizable backgrounds," *Phys. Rev. E*, vol. 58, pp. 3909–3915, Sep 1998.
- [28] J. O. Vargas and R. Adriano, "Subspace-based conjugate-gradient method for solving inverse scattering problems," *IEEE Trans. Antennas Propag.*, vol. 70, no. 12, pp. 12139–12146, 2022.
- [29] F.-F. Wang and Q. H. Liu, "A hybrid Born iterative Bayesian inversion method for electromagnetic imaging of moderate-contrast scatterers with piecewise homogeneities," *IEEE Trans. Antennas Propag.*, vol. 70, no. 10, pp. 9652–9661, 2022.
- [30] H. F. Arnoldus, "Representation of the near-field, middle-field, and far-field electromagnetic Greens functions in reciprocal space," *JOSA B*, vol. 18, no. 4, pp. 547–555, 2001.
- [31] Y. Chen, H. Zhang, T. J. Cui, F. L. Teixeira, and L. Li, "A mesh-free 3-d deep learning electromagnetic inversion method based on point clouds," *IEEE Trans. Microwave Theory Tech.*, vol. 71, no. 8, pp. 3530–3539, 2023.
- [32] D. A. Beard and T. Schlick, "Inertial stochastic dynamics. i. long-time-step methods for langevin dynamics," *The Journal of Chemical Physics*, vol. 112, no. 17, pp. 7313–7322, 2000.
- [33] N. Rahaman, A. Baratin, D. Arpit, F. Draxler, M. Lin, F. Hamprecht, Y. Bengio, and A. Courville, "On the spectral bias of neural networks," in *International conference on machine learning*, pp. 5301–5310, PMLR, 2019.
- [34] A. Vaswani, N. Shazeer, N. Parmar, J. Uszkoreit, L. Jones, A. N. Gomez, L. Kaiser, and I. Polosukhin, "Attention is all you need," *Advances in neural information processing systems*, vol. 30, 2017.
- [35] C. Finlay, J.-H. Jacobsen, L. Nurbekyan, and A. M. Oberman, "How to train your neural ode," *arXiv preprint arXiv:2002.02798*, vol. 2, 2020.
- [36] B. Lin, F. Gao, S. Zhang, T. Zhou, and A. Alkhateeb, "Deep learning-based antenna selection and csi extrapolation in massive MIMO systems," *IEEE Trans. Wireless Commun.*, vol. 20, no. 11, pp. 7669–7681, 2021.
- [37] G. Huang, Z. Liu, L. Van Der Maaten, and K. Q. Weinberger, "Densely connected convolutional networks," in *Proceedings of the IEEE conference on computer vision and pattern recognition*, pp. 4700–4708, 2017.
- [38] W. Grathwohl, R. T. Q. Chen, J. Bettencourt, I. Sutskever, and D. Duvenaud, "Ffjord: Free-form continuous dynamics for scalable reversible generative models," 2018.
- [39] M. Tancik, P. P. Srinivasan, B. Mildenhall, S. Fridovich-Keil, N. Rahaman, U. Singhal, R. Ramamoorthi, J. T. Barron, and R. Ng, "Fourier features let networks learn high frequency functions in low dimensional domains," 2020.
- [40] P. Ramachandran, B. Zoph, and Q. V. Le, "Searching for activation functions," *arXiv preprint arXiv:1710.05941*, 2017.
- [41] M. Grant and S. Boyd, "CVX: Matlab software for disciplined convex programming, version 2.1." <http://cvxr.com/cvx>, Mar. 2014.
- [42] Z.-q. Luo, W.-k. Ma, A. M.-c. So, Y. Ye, and S. Zhang, "Semidefinite relaxation of quadratic optimization problems," *IEEE Signal Process. Mag.*, vol. 27, no. 3, pp. 20–34, 2010.
- [43] A. M. Molaei, T. Fromenteze, V. Skourliakou, T. V. Hoang, R. Kumar, V. Fusco, and O. Yurduseven, "Development of fast fourier-compatible image reconstruction for 3d near-field bistatic microwave imaging with dynamic metasurface antennas," *IEEE Trans. Vehi. Tech.*, vol. 71, no. 12, pp. 13077–13090, 2022.
- [44] A. X. Chang, T. Funkhouser, L. Guibas, P. Hanrahan, Q. Huang, Z. Li, S. Savarese, M. Savva, S. Song, H. Su, *et al.*, "Shapenet: An information-rich 3D model repository," *arXiv preprint arXiv:1512.03012*, 2015.
- [45] X. Millard and Q. H. Liu, "Simulation of near-surface detection of objects in layered media by the BCGS-FFT method," *IEEE Trans. Geosci. Remote Sens.*, vol. 42, no. 2, pp. 327–334, 2004.
- [46] Y. Jiang and F. Gao, "Electromagnetic channel model for near field MIMO systems in the half space," *IEEE Commun. Lett.*, vol. 27, no. 2, pp. 706–710, 2023.